



Article

Boosting Capacity Performance of Bio-Waste Lignin-Derived Hierarchical Porous Carbon with Self-Doped Oxygen-Heteroatoms

Jia Liu *, Xiuwen Mei and Feng Peng *

Beijing Key Laboratory of Lignocellulosic Chemistry, MOE Engineering Research Center of Forestry Biomass Materials and Bioenergy, Beijing Forestry University, Beijing 100083, China

* Correspondence: liujia89@bjfu.edu.cn (J.L.); fengpeng@bjfu.edu.cn (F.P.)

Abstract: Herein, oxygen-doped hierarchical porous carbon (OHPC) is successfully fabricated derived from industrial-waste lignin. The as-obtained OHPC is endowed with not only high specific surface area and favorable pore size distribution for accessible ion diffusion and surface charge storage, but also high surface oxygen content (10.78%) for redox pseudocapacitance contributions. With these multiple advantages, the OHCP electrode demonstrates a high specific capacitance of 258 F g^{-1} at 0.5 A g^{-1} based on a three-electrode configuration, with a calculated pseudocapacitance contribution up to 19%. Furthermore, the assembled symmetric supercapacitor with OHPC also delivers an extremely superior electrochemical performance with outstanding rate capability, impressive cyclic stability (97.5% capacitance retention over 10,000 times under 2 A g^{-1}), and a high energy density of 9.27 Wh kg^{-1} at 25 W kg^{-1} . This work provides fresh insights into the high-value utilization of bio-waste lignin and promises great potential in the development of high-performance electrode materials for energy storage.



Citation: Liu, J.; Mei, X.; Peng, F. Boosting Capacity Performance of Bio-Waste Lignin-Derived Hierarchical Porous Carbon with Self-Doped Oxygen-Heteroatoms. *Batteries* **2022**, *8*, 286. <https://doi.org/10.3390/batteries8120286>

Academic Editor: Seiji Kumagai

Received: 17 November 2022

Accepted: 9 December 2022

Published: 13 December 2022

Publisher's Note: MDPI stays neutral with regard to jurisdictional claims in published maps and institutional affiliations.



Copyright: © 2022 by the authors. Licensee MDPI, Basel, Switzerland. This article is an open access article distributed under the terms and conditions of the Creative Commons Attribution (CC BY) license (<https://creativecommons.org/licenses/by/4.0/>).

1. Introduction

The continual increase in portable devices and electric vehicles propels the rapid development in energy storage devices [1–3]. As one of the promising systems, supercapacitors have attracted significant attention owing to their extremely high power density and long cycle lifespan [4–6]. Generally, the energy is electrostatically stored in supercapacitors by accumulating charges on the electrode surface [7–9]. The characteristics of electrode materials, therefore, directly dictate the electrochemical performance of supercapacitors [10]. Porous carbon materials are regarded as the most promising electrode candidates owing to their high specific surface area (SSA), superior electronic conductivities, and excellent structure stabilities [11–13]. Unfortunately, conventional porous carbon is expensive. The reported cost of carbon materials is as high as between EUR 10–20 per kg^{-1} , which is the most expensive component in supercapacitors and, thus, restricts their large-scale application in the future [14]. In this regard, to achieve sustainable development and market competition advantage for supercapacitors, low-cost synthesis strategies for porous carbon electrodes are a critical priority.

Thanks to the sustainability, easy availability, and low-cost of renewable biomass resources, they have gradually captured attention as alternative options [15–18]. Noteworthy, these biomasses are always rich in heteroatoms, such as oxygen, nitrogen, sulfur, and other elements, that make them promising precursors of self-doped carbonaceous materials [19–21]. Actually, heteroatom-doping can not only intensify the conductivity and surface wettability of porous carbon, but also provide additional pseudocapacitance to increase the energy density of supercapacitors [22–24]. Numerous biomass materials and

their derivatives, such as bamboo, ginkgo leaf, shrimp shells, cellulose, chitosan, lignin, etc., have been designed to prepare porous carbon [25–29]. Lignin is a kind of complicated aromatic polymer and natural biological macromolecule, inferior only to cellulose. Despite its high reserves, only a very small amount of lignin has been high-value utilized for the production of functional materials and chemicals. Most lignin resources are commonly regarded as wastes or pollutants of pulp-making and biorefinery [30,31]. In addition, from the aspect of chemical structure, lignin chemically contains a higher carbon content (up to 60 wt%) compared to the polysaccharide or holocellulose fraction, as well as abundant oxygen-containing moieties (such as hydroxyl and carboxyl groups), rendering it an advanced source for oxygen-doped porous carbon materials [32,33]. Therefore, the utilization of commercially discarded lignin to prepare high-value porous carbon is of great significance for sustainable development and circular economy. Nevertheless, the 3D amorphous branches of lignin can easily induce intermolecular crosslinking interactions and form a compact stacked structure to a considerable extent, resulting in unfavorable porosity texture and low surface area during the direct process of carbonization [34,35]. Until now, some effective strategies, such as microwave-assisted and bacterial activation methods, have been previously reported to prepare the porous carbon with high SSA. However, these manipulations are always complicated and high-cost, preventing large-scale application [36,37]. Moreover, different from the organosolv lignin that usually has a high β-O-4 content, industrial lignin is highly condensed and crosslinked with strong C–C bonds among most of lignin monomers [38]. Such structural characteristics always lead to relatively poor concentration of oxygen heteroatoms in lignin-derived carbon materials, bringing about insufficient pseudocapacitance contribution and unsatisfactory capacitance [39–41].

In this contribution, through a facile two-step method, a high content oxygen-doped hierarchical porous carbon material (OHPC) from commercial bio-waste lignin was successfully fabricated. The as-obtained OHPC not only showed a hierarchical porous structure with an interconnected network and high SSA of $1289.7 \text{ m}^2 \text{ g}^{-1}$, but also a high concentration of O heteroatoms (up to 10.78%), contributing to wettability between the electrode/electrolyte interface and pseudocapacitance behaviors. Consequently, the OHPC exhibited a high specific capacitance of 258 F g^{-1} at 0.5 A g^{-1} on a three-electrode configuration, with a high pseudocapacitance contribution up to 19%. As for the symmetric supercapacitor, the specific gravimetric capacitance of 250 F g^{-1} at 0.5 A g^{-1} with only 2.5% fading after 10,000 cycles and superior cycling durability of 97.5% capacitance retention over 10,000 cycles was demonstrated. More specifically, a high energy density of 9.27 Wh kg^{-1} at 25 W kg^{-1} was also achieved.

2. Materials and Methods

2.1. Chemical

The lignin used in this work was obtained from Longlive Biotechnology Co., Ltd., Dezhou, China. Potassium hydroxide (KOH) was purchased from Shanghai Macklin Biochemical Co., Ltd. Both the hydrochloric acid (HCl) and phosphoric acid (H_3PO_4) were purchased from Beijing Chemical Works. The Super-P and PTFE were purchased from Shenzhen Kejing Star Technology Co., Ltd., Yuncheng, China. All reagents were used as received without further purification.

2.2. Preparations of OHPCs

Before the preparation of OHPCs, the lignin precursor was successively purified with 0.1 M HCl and deionized water, and then was dried in an oven (ZXRD-A5110, Shanghai Zhicheng Analytical Instrument Manufacturing Co., Ltd., Shanghai, China) at 60°C for 24 h. Afterwards, the OHPCs were synthesized through a two-step activation method. Firstly, 6 g of lignin was infiltrated in 15 g of 20 wt% H_3PO_4 solution for 12 h, then the mixture was dried at 100°C for 24 h and annealed in a muffle furnace (SX2-4-10, Tianjin Zhonghuan Experiment Electric Furnace Co., Ltd., Tianjin, China) at 400°C for 1 h in air atmosphere to obtain H_3PO_4 -assisted pre-carbonized intermediate char products. Subsequently, the

intermediate products were washed by 1 M HCl (100 °C) and hot water (70–80 °C) several times until neutral pH. After drying at 100 °C for 12 h, the dried char was immersed into 30 wt% KOH solution with a 2:1 ratio of KOH to carbon, respectively, and was subsequently burned at 700 °C for 1 h in a tube furnace (Tianjin Zhonghuan Experiment Electric Furnace Co., Ltd., Tianjin, China). Finally, the collected materials were rinsed with 1 M HCl solution and then deionized water, followed by thorough drying at 100 °C for 24 h.

2.3. Material Characterizations

The morphologies of the samples were investigated by a field emission scanning electron microscope (FESEM, Hitachi SU8010, Hitachi Ltd., Tokyo, Japan). The microstructures of the samples were explored by X-ray powder diffraction (XRD, Bruker D8 ADVANCE at a scan rate of 5 °min⁻¹, Bruker, Ettlingen, Germany) and Raman scattering (HORIBA EVOLUTION, with 532 nm wavelength incident laser light and a power of 12 mW, Montpellier, France). The pore structure of the samples was characterized by N₂ adsorption isotherms using the Quantachrome Autosorb iQ system. The SSA was calculated from the Brunauer–Emmett–Teller (BET) plot of the nitrogen adsorption isotherm. The pore size distribution was determined by the Nonlocal Density Functional Theory (NLDFT) method. The chemical composition and chemical state of the surface were investigated by X-ray photoelectron spectroscopy (XPS, Thermo ESCALAB 250XI, Thermo Fisher Scientific, Waltham, MA, USA) with an Al K α radiation source.

2.4. Electrochemical Characterizations

The electrochemical measurements were conducted in three-electrode and two-electrode configurations in 6 M KOH. To prepare the working electrode, the OHPC active material (80 wt%), Super-p (10 wt%), and PTFE (10 wt%) were mixed to form a homogeneous slurry. The slurry was coated onto the surface of nickel foam and then dried at 100 °C for 4 h. Then, the as-prepared electrode disks were compacted at 10 MPa with a tablet machine and dried at 100 °C for 12 h. The active material loading was from 1.5–2.0 mg cm⁻². In the three-electrode system, the OHPC electrode was used as the working electrode, and the platinum foil and Hg/HgO electrode were used as the counter electrode and reference electrode, respectively. In the symmetric cell, two OHPC electrodes with the same mass loading and size were separated by a piece of filter paper. The cyclic voltammetry (CV), galvanostatic charge–discharge (GCD), and electrical impedance spectroscopy (EIS) tests were carried out on a CHI760E working station. The working voltages for both GCD and CV measurements were recorded between –1 and 0 V in a three-electrode system and between 0 and 1 V in the two-electrode system, respectively. The EIS measurements were carried out with open-circuit potential under a frequency between 100 kHz and 10 mHz with an amplitude of 5 mV, and the impedance data was fitted by using ZSimpWin software.

The gravimetric capacitances were calculated according to the discharge curves of GCD based on the following equation:

$$C_g = \frac{nI\Delta t}{m\Delta V} \quad (1)$$

where C_g is the gravimetric capacitance, F g⁻¹, I is the discharge current, A, m is mass of active materials, and g , Δt (s) and ΔV (V) is the discharge time and potential change within Δt after IR drop, respectively. n is the coefficient number in which $n = 1$ for the three-electrode system and $n = 2$ for symmetrical cells.

The energy density E (Wh kg⁻¹) and power density P (W kg⁻¹) of the symmetric devices based on two electrodes are calculated by the following equation:

$$E_g = C_{cell}\Delta V^2 / (2 \times 3.6) = C_g\Delta V^2 / (4 \times 2 \times 3.6) \quad (2)$$

$$P_g = 3600E_g / \Delta t \quad (3)$$

The volumetric capacitance was determined by Equation (2) as follows:

$$C_v = C_g \rho \quad (4)$$

$$\rho = 1 / (V_{total} + 1/\rho_{carbon}) \quad (5)$$

where C_v is the specific volumetric capacitance, $F\text{ cm}^{-3}$; ρ is the density of OHPC-T materials, $g\text{ cm}^{-3}$; ρ_{carbon} is the true density of carbon materials and the value is 2 g cm^{-3} [42]; V_{total} is the total pore volume of OHPC, $\text{cm}^3\text{ g}^{-1}$.

The capacitance of the cell is dependent on the frequency $C(\omega)$ which can be evaluated in the impedance spectrum and defined as follows:

$$C = C'(\omega) - jC''(\omega) \quad (6)$$

$$C'(\omega) = -Z''(\omega) / (\omega|Z(\omega)|)^2 \quad (7)$$

$$C''(\omega) = Z'(\omega) / (\omega|Z(\omega)|)^2 \quad (8)$$

where the ω is angular frequency and calculated by $\omega = 2\pi f$; $C'(\omega)$ represents the real part of $C(\omega)$; $C''(\omega)$ is the virtual part corresponding to the loss of energy dissipation and frequency; $Z(\omega)$ is the complex impedance of the cell in which $Z'(\omega)$ and $-Z''(\omega)$ represent its real and imaginary part, respectively.

3. Results

The OHPC sample was synthesized using a facile two-step approach comprising of low-temperature H_3PO_4 pre-activation and KOH activation, and the detailed preparation strategy is analyzed in Figure S1. The surface morphology of the lignin precursor and as-prepared OHPC were characterized by SEM images. As shown in Figure S2, the lignin precursor exhibited a typical bulk structure composed of agglomerated particles. After activation, the as-obtained OHPC displayed loose and rough morphologies with an interconnected porous network (Figure 1a). Such special porous features can offer not only available active sites for charge storage but also accessible channels for ion transport, rendering excellent energy storage capability.

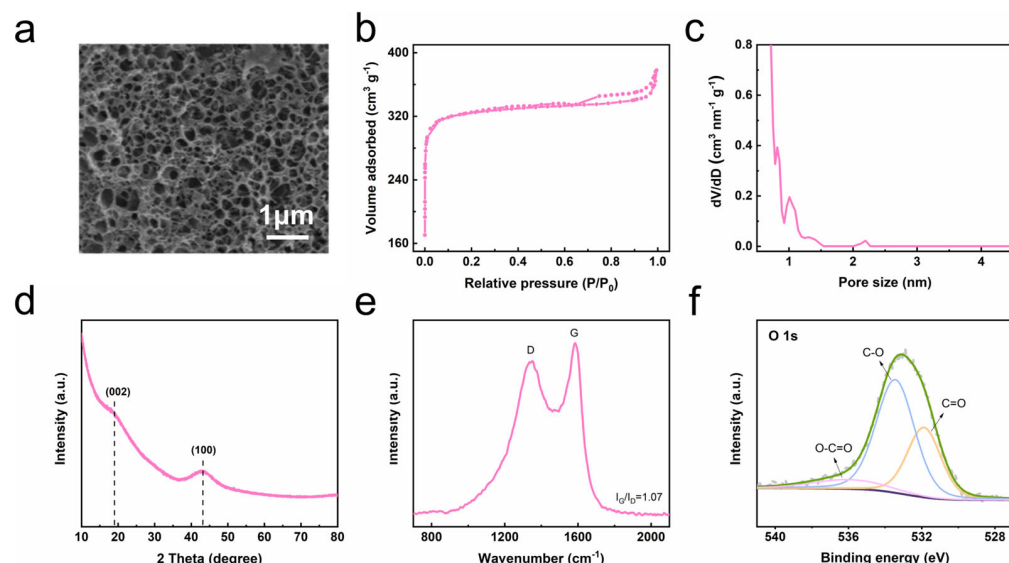
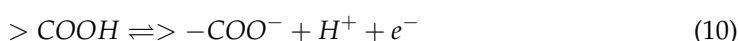
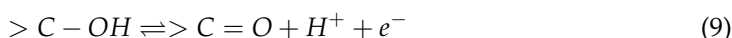


Figure 1. The physicochemical properties of OHPC. (a) SEM image; (b) N_2 adsorption–desorption isotherm; (c) Pore size distribution; (d) XRD pattern; (e) Raman spectrum; (f) High-resolution O1s XPS spectrum.

To further gain insight into the textural properties of OHPC samples, N₂ adsorption-desorption measurements were performed. The isotherm presented a typical I isotherm with H4 hysteresis loop ($0.48 \leq P/P_0 \leq 0.98$), suggesting that the OHPC was endowed with a hierarchical micro-mesoporous structure (Figure 1b). Remarkably, close observation in pore size distributions (Figure 1c) showed distinctly bimodal peaks from 1–2 nm and from 2–5 nm, respectively, which belonged to micropores and mesopores, further confirming the hierarchical porous properties of the OHPC. The specific BET surface area of the OHPC was calculated to be as large as $1289.7 \text{ m}^2 \text{ g}^{-1}$. The hierarchical porous structure with high SSA would offer sufficient contact area between the electrode and electrolyte, ensuring high availability of active sites, thus, attaining the OHPC as advanced electrodes for supercapacitors to enhance the power characteristics.

The XRD pattern of the OHPC sample (Figure 1d) depicted two diffraction peaks located at approximately 19° and 43° , respectively, which can be assigned to the (002) and (100) crystalline planes of graphite carbon, indicating the successful fabrication of the OHPC with some graphitization features [43,44]. Raman spectrum (Figure 1e) indicated that the OHPC displayed two broader peaks. The G band located at 1580 cm^{-1} corresponded to a graphitic characteristic, and the D band at approximately 1350 cm^{-1} belonged to a disordered and defective graphitic structure. The intensity ratio of the G band to D band (I_G/I_D) represented the graphitization degree of the carbon materials. The I_G/I_D value for OHPC was demonstrated to be 1.07, suggesting the relatively high degree of graphitization, which can help fast electronic transfer behaviors during cycling.

Further investigations on surface element composition and bonding characteristics of OHPC were conducted by XPS. As expected, the survey spectrum of OHPC verified the co-existence of C and O elements with a high concentration of O dopants as high as 10.78% (Figure S3 and Table S1), indicating the successful doping of the O heteroatom into lignin-derived OHPC. The high-resolution C 1s spectrum (Figure S4) could be deconvoluted into five peaks as follows: C=C–C (284.75 eV), C–O (285.65 eV), C=O (286.60 eV), O–C=O (287.85 eV), and $\pi-\pi^*$ interaction (289.40 eV). The O1s spectrum (Figure 1f) showed three peaks located at 531.8 eV, 533.4 eV, and 536.3 eV, respectively, corresponding to C=O bonds, bridge-bonded oxygen (C–O in C–O–H, C–O–C), and ester groups (O–C=O) [45]. These oxygen-functionalization groups not only promote the hydrophilic property of the OHPC electrode in aqueous electrolytes, but also contribute to pseudocapacitance behaviors during charge/discharge cycling based on the following redox reactions (Equations (9)–(11)) [46], consequently increasing capacitance performance. Notably, considering the basic electrolyte (6M KOH) used in this work, Equations (9) and (10) actually represent a quasi-reversible and irreversible property, while Equation (11) contributes the main pseudocapacitive characteristics.



The electrochemical performances of the OHPC electrode were evaluated in a supercapacitor with a three-electrode system. Figure 2a presents the CV curve of OHPC at a scan rate of 5 mV s^{-1} , which possessed quasi-rectangular shapes with Faradaic peaks between -1 and -0.2 V , ascribing to pseudocapacitance contribution generated by oxygen-containing functional groups, which was consistent with the XPS results aforementioned. The rate-dependent CV curves of OHPC at sweep rates varied from 5 to 200 mV s^{-1} , recorded in Figure S5(a). All the CV curves retained quasi-rectangular shapes with only slightly broadened humps even at a high rate of 200 mV s^{-1} , which further demonstrated the superior capacitance behavior and rate performance of the as-prepared OHPC electrode. Furthermore, the excellent capacitive behavior can also be reflected by the relationship between the peak current response (i) and the sweep rate (v) (in Figure S6), which shows that the parameter b -value is close to 1, indicative of the fast near-surface activities [47–49].

Notably, the impedance spectrum in Figure 2b exhibits a nearly vertical line, further demonstrating the ideal surface-controlled capacitive behaviors. At the high frequency region, the semicircle is correlated with the charge transfer process at the electrode/electrolyte interface and the resistance arising from the Faradaic redox [50,51]. The value of charge transfer resistance (R_{ct}) for OHPC was determined to be only $0.72\ \Omega$, respectively, suggesting the fast charge transfer kinetics of OHPC electrodes.

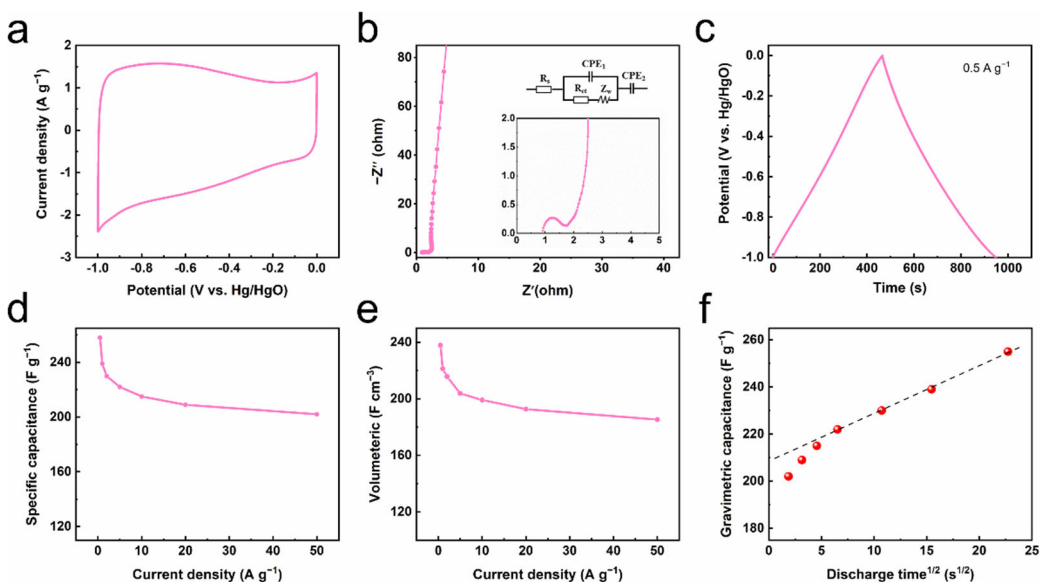


Figure 2. Electrochemical performance of OHPC electrodes tested in a three-electrode configuration. (a) CV curve at 5 mV s^{-1} ; (b) Nyquist plots (inset magnified $0\text{--}5\ \Omega$ region); (c) GCD curves at 0.5 A g^{-1} ; (d,e) Gravimetric and volumetric rate performance from 0.5 to 50 A g^{-1} ; (f) Gravimetric capacitance of OHPC vs. $T^{1/2}$ using the capacitance from 0.5 to 50 A g^{-1} , and the dashed diagonal line represents the extrapolation of the infinite sweep rate ($T \rightarrow 0$).

Figure 2c depicts the GCD plots of OHPC performance at 0.5 A g^{-1} , of which the symmetric curves with weak deviation from a triangular shape are clearly identified, verifying the contribution of pseudocapacitance attributed to the oxygen-containing functional groups. The GCD profiles of OHPC at different rates (from 10 A g^{-1} to 50 A g^{-1}) exhibited highly linear symmetry, which demonstrates the OHPC electrode had excellent electrochemical reversibility (Figure S5b). The gravimetric capacitance properties and volumetric capacitance derived from the GCD curves are shown in Figure 2d,e. The OHPC offered a high gravimetric specific capacitance of 258 F g^{-1} and volumetric capacitance of 232 F cm^{-3} at 0.5 A g^{-1} , with 80% gravimetric capacitive retention even at 50 A g^{-1} . For comparison, the capacitance performance of the porous carbon electrode by direct KOH activation of lignin at $700\text{ }^{\circ}\text{C}$ is also measured in Figure S7. Evidently, the supercapacitor assembled from porous carbon generated by the direct activation of lignin showed a poor electrochemical performance. For example, the lignin-derived porous carbon electrode showed an initial specific capacitance of 207 F g^{-1} at 0.5 A g^{-1} , which was only 0.8 -fold of that achieved for the OHPC electrode. The significant improvement in capacitance characteristics of the OHPC electrode is mainly attributed to the synergistic effects of high surface area, favourable pore size distribution, and functionalized oxygen-doped species, effectively affording accessible charge transfer paths and ion diffusion channels, available active sites for charge storage, high pseudocapacitance contribution and good wettability at the electrode/electrolyte interface. Notably, such high capacitance properties with excellent rate capability of OHPC is also more superior than those previously reported works of lignin-derived carbon-based electrodes, as shown in Table S2, further successfully demonstrating the validity of the as-obtained OHPC as an electrode in supercapacitors [36,37,52–63].

To further investigate the properties of the charge storage process, the electrochemical kinetics of OHPC was analyzed. It is known that the capacitance (C) can be calculated by Equation (12) [60,64]:

$$C = k_1 + k_2 T^{1/2} \quad (12)$$

where T is the discharge time derived from GCD tests, s. k_1 and $k_2 T^{1/2}$ correspond to the current contribution from surface capacitive effect (classically attributed to double-layer capacitance: $T \rightarrow 0$) and diffusion-limited component dominated by the charge/discharge rate ($T \rightarrow \infty$), respectively. Figure 2f plots the relationship of the discharge time and specific capacitance of OHPC between 0.5 and 50 A g⁻¹. The $k_2 T^{1/2}$ term represents the long- T data, which extrapolates to k_1 at the $T^{1/2} = 0$ intercept. Apparently, double-layer capacitance contributing to a gravimetric capacitance is calculated to be 208 F g⁻¹, with a ratio of approximately 81%. That means the OHPC showed a high pseudocapacitance contribution to capacitance of up to 19%, further demonstrating its superiority as an advanced electrode in supercapacitors.

To investigate the practical applicability of the OHPC electrode, a symmetric supercapacitor configuration was fabricated, and the corresponding electrochemical performances are shown in Figure 3. The symmetrical supercapacitor based on OHPC (OHPC//OHPC) was assembled into a CR2032 coin cell. Figure 3a illustrates the comparative CV curves of OHPC//OHPC at different scan rates, of which the quasi-rectangular shapes without apparent distortion were clearly observed even at a high scan rate of 200 mV s⁻¹. The GCD curves (Figure 3b,c) cycled at varied current densities from 0.5 to 50 A g⁻¹ are nearly triangular-shaped and symmetrical, suggesting the ideal capacitive behavior of the OHPC electrode. The rate performances achieved at different current densities are shown in Figure 3d, giving an impressive electrode capacitance of 250 F g⁻¹ at the current density of 0.5 A g⁻¹. Even at 50 A g⁻¹, the capacitance could still achieve 200 F g⁻¹ with a high capacitance retention of 79.8%. All these results were consistent with those obtained in the three-electrode system, successfully demonstrating the reliability of the versatile fabrication process in this article.

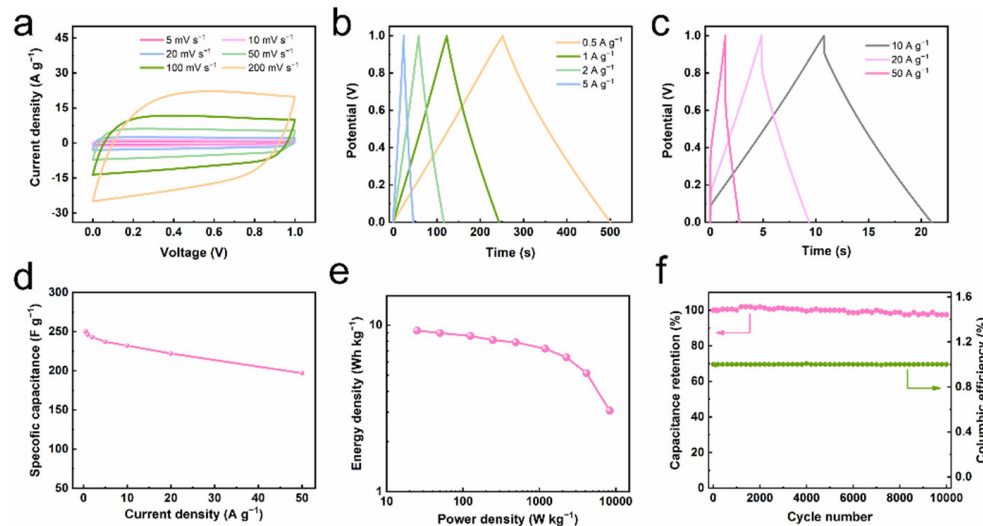


Figure 3. Electrochemical performance of OHPC//OHPC supercapacitors. (a) CV curves at the scan rate from 5 to 200 mV s⁻¹; (b,c) GCD curves from 0.5 A g⁻¹ to 50 A g⁻¹; (d) Rate performance tested from 0.5 to 50 A g⁻¹; (e) Ragone plot; (f) Cyclic stability and columbic efficiency after 10,000 cycles at 2 A g⁻¹.

The Ragone plot in Figure 3e illustrates that the as-fabricated OHPC//OHPC configuration delivered a high gravimetric energy density of 9.27 Wh kg⁻¹ at a gravimetric power density of 25 W kg⁻¹ and retained 3.06 Wh kg⁻¹ even at 8345 W kg⁻¹, having a slight advantage to most of the lignin-derived carbon-based symmetric supercapacitors with a 6 M KOH electrolyte, especially considering the economic benefits (Table S2) [37,52,53,58,60,62].

For example, the best reported energy density by other works is 13.5 Wh kg^{-1} for ordered mesoporous carbons from organosolv lignin, only 31% higher than our current results [57]. Unfortunately, the extraction of organosolv lignin generally requires quantities of organic solvent under high temperature and pressure conditions, inducing significant increase in cost. In addition, the excellent performance was also reflected by the cyclic stability testing in Figure 3f, which indicates that the capacitance retention can still be kept as high as 97.5% even after 10,000 successive cycles with a high Coulombic efficiency of approximately 100%, demonstrating its exceptional cycling stability.

The EIS measurement of OHPC//OHPC was conducted to further investigate the capacitance performance. From the Bode phase diagram (Figure 4a), the phase degree could achieve 86.4° , suggesting that the OHPC exhibited a good capacitive characteristic. The evolution of normalized $C'(\omega)$ and $C''(\omega)$ versus frequencies is revealed in Figure 4b. When the normalized $C'(\omega)$ achieved 0.5, the operating frequency (f_0) and relaxation time constant ($\tau_0 = 1/f_0$) could be obtained. Actually, the τ_0 is a quantitative parameter used to evaluate the charge and discharge rate of devices. As presented in Figure 4b, the cell had an operating frequency of 0.36 Hz, corresponding to a short τ_0 of 2.78 s, successfully indicating the fast response of OHPC//OHPC devices [65].

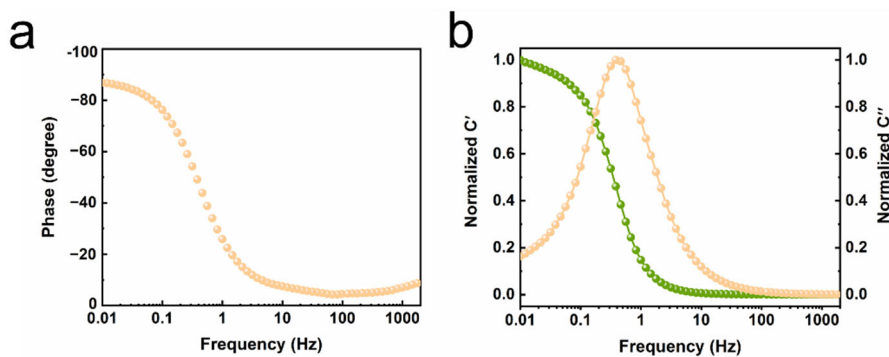


Figure 4. The EIS measurement of OHPC//OHPC symmetric supercapacitors. (a) Bode plot and (b) the normalized real and virtual part capacitance of the OHPC//OHPC.

Based on the above discussions, the primary attributes regarding high performance OHPC can be concluded. Firstly, it has flexible tunability. By adjusting the reaction parameters, such as the amounts of reactants, the calcination temperatures, and the type of precursors, the properties of the resulting carbon material can be easily tuned, which directly determines the electrochemical performance of the supercapacitors (Figures S8 and S9). Secondly, it has social and economic benefits. Approximately 50 million tons of industrial lignin are produced each year from the boiling waste of the pulp and paper industry and the residues from the preparation of fuel ethanol. Of these, more than 95% of lignin is burned after concentration or discarded directly, causing environmental pollution and resource wastage [66]. The application of bio-waste lignin as a high-value electrode material for supercapacitors is important for harmonizing the sustainable development path of the environment, economy, and society.

4. Conclusions

The utilization of industrial lignin as a feedstock to prepare high-value chemicals or products for energy storage renders great significance in environmental sustainability and economic viability. However, the high-branched structure of lignin leaves its derived carbon materials with insufficient porous properties and low SSA, leading to poor compatibility with energy storage devices. In this work, an advanced self-doped OHPC electrode derived from bio-waste lignin has been synthesized for supercapacitors. The resultant OHPC has a hierarchical interconnected porous architecture, large SSA, and a high content of oxygen, which not only provides available ion diffusion channels and abundant active sites but also favors high pseudocapacitance contributions (up to 19%). All these favorable advantages

benefit the OHPC with excellent capacitance properties and rate performances in both three-electrode and two-electrode systems. In particular, the symmetric supercapacitor delivers an extremely superior capacitance performance with outstanding rate capability (79.8% retention at high current density of 50 A g^{-1}) and impressive cycling stability (97.5% capacitance retention over 10,000 cycles). This study opens an effective path to convert abundant, sustainable, and renewable bio-waste lignin into advanced hierarchical porous carbon as high-performance electrode material for supercapacitors.

Supplementary Materials: The following supporting information can be downloaded at <https://www.mdpi.com/article/10.3390/batteries8120286/s1>. Figure S1: Schematic representation of the synthetic strategy of lignin-derived OHPC; Figure S2: SEM image of the raw lignin particles; Figure S3: XPS survey spectrum of OHPC. Figure S4: High-resolution C1s XPS spectrum of OHPC material; Figure S5: (a) The rate-dependent CV curves of OHPC at scan rates varying from 5 to 200 mV s^{-1} , (b) The GCD profiles of OHPC at different rates from 10 A g^{-1} to 50 A g^{-1} ; Figure S6: b-value determination of the anodic peak current density shows that this value is approximately 1; Figure S7: The capacitance performance of the porous carbon electrode by direct KOH activation of lignin at $700 \text{ }^{\circ}\text{C}$; Figure S8: The SEM images of lignin-derived hierarchical porous carbon calcinated at different temperatures (a) $800 \text{ }^{\circ}\text{C}$ and (b) $900 \text{ }^{\circ}\text{C}$; Figure S9: The gravimetric rate performance of lignin-derived hierarchical porous carbon calcinated at $800 \text{ }^{\circ}\text{C}$ and $900 \text{ }^{\circ}\text{C}$ from 0.5 to 50 A g^{-1} ; Table S1: The element concentration of OHPC sample; Table S2: Comparison of electrochemical performances for the lignin-based carbon materials.

Author Contributions: J.L.: Conceptualization, Supervision, Writing—original draft; X.M.: Methodology, Investigation, Data Curation; F.P.: Conceptualization, supervision; Writing—Review and Editing. All authors have read and agreed to the published version of the manuscript.

Funding: This work was supported by the Beijing Forestry University Outstanding Young Talent Cultivation Project (2019JQ03017) and the National Science Fund for Distinguished Young Scholars (32225034), and China-111 Project (BP0820033).

Data Availability Statement: Not applicable.

Conflicts of Interest: The authors declare no conflict of interest.

References

1. Swain, N.; Tripathy, A.; Thirumurugan, A.; Saravanakumar, B.; Schmidt-Mende, L.; Ramadoss, A. A brief review on stretchable, compressible, and deformable supercapacitor for smart devices. *Chem. Eng. J.* **2022**, *446*, 136876. [[CrossRef](#)]
2. Liu, J.; Yuan, H.; Tao, X.; Liang, Y.; Yang, S.J.; Huang, J.Q.; Yuan, T.Q.; Titirici, M.M.; Zhang, Q. Recent progress on biomass-derived ecomaterials toward advanced rechargeable lithium batteries. *EcoMat* **2020**, *2*, e12019. [[CrossRef](#)]
3. Wang, G.; Zhang, L.; Zhang, J. A review of electrode materials for electrochemical supercapacitors. *Chem. Soc. Rev.* **2012**, *41*, 797–828. [[CrossRef](#)] [[PubMed](#)]
4. Zhang, L.L.; Zhao, X.S. Carbon-based materials as supercapacitor electrodes. *Chem. Soc. Rev.* **2009**, *38*, 2520–2531. [[CrossRef](#)]
5. Simon, P.; Gogotsi, Y. Perspectives for electrochemical capacitors and related devices. *Nat. Mater.* **2020**, *19*, 1151–1163. [[CrossRef](#)]
6. Liu, M.; Niu, J.; Zhang, Z.; Dou, M.; Wang, F. Potassium compound-assistant synthesis of multi-heteroatom doped ultrathin porous carbon nanosheets for high performance supercapacitors. *Nano Energy* **2018**, *51*, 366–372. [[CrossRef](#)]
7. Raza, W.; Ali, F.; Raza, N.; Luo, Y.; Kim, K.-H.; Yang, J.; Kumar, S.; Mehmood, A.; Kwon, E.E. Recent advancements in supercapacitor technology. *Nano Energy* **2018**, *52*, 441–473. [[CrossRef](#)]
8. Sharma, P.; Bhatti, T.S. A review on electrochemical double-layer capacitors. *Energy Convers. Manag.* **2010**, *51*, 2901–2912. [[CrossRef](#)]
9. Koda, K.; Taira, S.; Kubota, A.; Isozaki, T.; You, X.; Uraki, Y.; Sugimura, K.; Nishio, Y. Development of Lignin-Based Terpolyester Film and Its Application to Separator Material for Electric Double-Layer Capacitor. *J. Wood Chem. Technol.* **2019**, *39*, 199–214. [[CrossRef](#)]
10. Largeot, C.; Portet, C.; Chmiola, J.; Taberna, P.-L.; Gogotsi, Y.; Simon, P. Relation between the ion size and pore size for an electric double-layer capacitor. *J. Am. Chem. Soc.* **2008**, *130*, 2730–2731. [[CrossRef](#)]
11. Saikia, B.K.; Benoy, S.M.; Bora, M.; Tamuly, J.; Pandey, M.; Bhattacharya, D. A brief review on supercapacitor energy storage devices and utilization of natural carbon resources as their electrode materials. *Fuel* **2020**, *282*, 118796. [[CrossRef](#)]
12. Yin, J.; Zhang, W.; Alhebshi, N.A.; Salah, N.; Alshareef, H.N. Synthesis Strategies of Porous Carbon for Supercapacitor Applications. *Small Methods* **2020**, *4*, 1900853. [[CrossRef](#)]

13. Wang, Y.; Zhang, L.; Hou, H.; Xu, W.; Duan, G.; He, S.; Liu, K.; Jiang, S. Recent progress in carbon-based materials for supercapacitor electrodes: A review. *J. Mater. Sci.* **2021**, *56*, 173–200. [[CrossRef](#)]
14. Schuetter, C.; Pohlmann, S.; Balducci, A. Industrial Requirements of Materials for Electrical Double Layer Capacitors: Impact on Current and Future Applications. *Adv. Energy Mater.* **2019**, *9*, 1900334. [[CrossRef](#)]
15. Athanasiou, M.; Yannopoulos, S.N.; Ioannides, T. Biomass-derived graphene-like materials as active electrodes for supercapacitor applications: A critical review. *Chem. Eng. J.* **2022**, *446*, 137191. [[CrossRef](#)]
16. Mensah-Darkwa, K.; Zequine, C.; Kahol, P.K.; Gupta, R.K. Supercapacitor Energy Storage Device Using Biowastes: A Sustainable Approach to Green Energy. *Sustainability* **2019**, *11*, 414. [[CrossRef](#)]
17. Divyashree, A.; Hegde, G. Activated carbon nanospheres derived from bio-waste materials for supercapacitor applications—A review. *RSC Adv.* **2015**, *5*, 88339–88352. [[CrossRef](#)]
18. Shaker, M.; Ghazvini, A.A.S.; Cao, W.; Riahifar, R.; Ge, Q. Biomass-derived porous carbons as supercapacitor electrodes—A review. *New Carbon Mater.* **2021**, *36*, 546–568. [[CrossRef](#)]
19. Gopalakrishnan, A.; Raju, T.D.; Badhulika, S. Green synthesis of nitrogen, sulfur-co-doped worm-like hierarchical porous carbon derived from ginger for outstanding supercapacitor performance. *Carbon* **2020**, *168*, 209–219. [[CrossRef](#)]
20. Gang, X.; Krishnamoorthy, M.; Jiang, W.; Pan, J.; Pan, Z.; Liu, X. A novel in-situ preparation of N-rich spherical porous carbon as greatly enhanced material for high-performance supercapacitors. *Carbon* **2021**, *171*, 62–71. [[CrossRef](#)]
21. Yang, H.; Ye, S.; Zhou, J.; Liang, T. Biomass-Derived Porous Carbon Materials for Supercapacitor. *Front. Chem.* **2019**, *7*, 274. [[CrossRef](#)] [[PubMed](#)]
22. Gopalakrishnan, A.; Badhulika, S. Effect of self-doped heteroatoms on the performance of biomass-derived carbon for supercapacitor applications. *J. Power Sources* **2020**, *480*, 228830. [[CrossRef](#)]
23. Liu, H.; Liu, R.; Xu, C.; Ren, Y.; Tang, D.; Zhang, C.; Li, F.; Wei, X.; Zhang, R. Oxygen-nitrogen-sulfur self-doping hierarchical porous carbon derived from lotus leaves for high-performance supercapacitor electrodes. *J. Power Sources* **2020**, *479*, 228799. [[CrossRef](#)]
24. Shen, F.; Zhu, L.; Qi, X. Nitrogen Self-Doped Hierarchical Porous Carbon from Myriophyllum Aquaticum for Supercapacitor Electrode. *ChemistrySelect* **2018**, *3*, 11350–11356. [[CrossRef](#)]
25. Tian, W.; Gao, Q.; Tan, Y.; Yang, K.; Zhu, L.; Yang, C.; Zhang, H. Bio-inspired beehive-like hierarchical nanoporous carbon derived from bamboo-based industrial by-product as a high performance supercapacitor electrode material. *J. Mater. Chem. A* **2015**, *3*, 5656–5664. [[CrossRef](#)]
26. Zhu, X.; Yu, S.; Xu, K.; Zhang, Y.; Zhang, L.; Lou, G.; Wu, Y.; Zhu, E.; Chen, H.; Shen, Z.; et al. Sustainable activated carbons from dead ginkgo leaves for supercapacitor electrode active materials. *Chem. Eng. Sci.* **2018**, *181*, 36–45. [[CrossRef](#)]
27. Mondal, A.K.; Kretschmer, K.; Zhao, Y.; Liu, H.; Fan, H.; Wang, G. Naturally nitrogen doped porous carbon derived from waste shrimp shells for high-performance lithium ion batteries and supercapacitors. *Micropor. Mesopor. Mat.* **2017**, *246*, 72–80. [[CrossRef](#)]
28. Huang, J.; Wu, J.; Dai, F.; Li, C.M. 3D honeycomb-like carbon foam synthesized with biomass buckwheat flour for high-performance supercapacitor electrodes. *Chem. Commun.* **2019**, *55*, 9168–9171. [[CrossRef](#)]
29. Li, Y.; Zhang, D.; He, J.; Wang, Y.; Zhang, X.; Zhang, Y.; Liu, X.; Wang, K.; Wang, Y. Hierarchical porous carbon nanosheet derived from waste engine oil for high-performance supercapacitor application. *Sustain. Energ. Fuels* **2019**, *3*, 499–507. [[CrossRef](#)]
30. Zhang, W.; Yin, J.; Wang, C.; Zhao, L.; Jian, W.; Lu, K.; Lin, H.; Qiu, X.; Alshareef, H.N. Lignin Derived Porous Carbons: Synthesis Methods and Supercapacitor Applications. *Small Methods* **2021**, *5*, e2100896. [[CrossRef](#)]
31. Zhang, R.; Du, Q.; Wang, L.; Zheng, Z.; Guo, L.; Zhang, X.; Yang, X.; Yu, H. Unlocking the response of lignin structure for improved carbon fiber production and mechanical strength. *Green Chem.* **2019**, *21*, 4981–4987. [[CrossRef](#)]
32. Khamnantha, P.; Homla-or, C.; Suttisintong, K.; Manyam, J.; Raita, M.; Champreda, V.; Intasanta, V.; Butt, H.-J.; Berger, R.; Pangon, A. Stable Lignin-Rich Nanofibers for Binder-Free Carbon Electrodes in Supercapacitors. *ACS Appl. Nano Mater.* **2021**, *4*, 13099–13111. [[CrossRef](#)]
33. Thongsai, N.; Hrimchum, K.; Aussawasathien, D. Carbon fiber mat from palm-kernel-shell lignin/polyacrylonitrile as intrinsic-doping electrode in supercapacitor. *Sustain. Mater. Technol.* **2021**, *30*, e00341. [[CrossRef](#)]
34. Fu, F.; Wang, H.; Yang, D.; Qiu, X.; Li, Z.; Qin, Y. Lamellar hierarchical lignin-derived porous carbon activating the capacitive property of polyaniline for high-performance supercapacitors. *J. Colloid Interface Sci.* **2022**, *617*, 694–703. [[CrossRef](#)]
35. Li, W.; Wang, G.; Sui, W.; Xu, T.; Li, Z.; Parvez, A.M.; Si, C. Facile and scalable preparation of cage-like mesoporous carbon from lignin-based phenolic resin and its application in supercapacitor electrodes. *Carbon* **2022**, *196*, 819–827. [[CrossRef](#)]
36. Zhang, K.; Liu, M.; Zhang, T.; Min, X.; Wang, Z.; Chai, L.; Shi, Y. High-performance supercapacitor energy storage using a carbon material derived from lignin by bacterial activation before carbonization. *J. Mater. Chem. A* **2019**, *7*, 26838–26848. [[CrossRef](#)]
37. Chen, W.; Luo, M.; Yang, K.; Zhou, X. Microwave-assisted KOH activation from lignin into hierarchically porous carbon with super high specific surface area by utilizing the dual roles of inorganic salts: Microwave absorber and porogen. *Micropor. Mesopor. Mater.* **2020**, *300*, 110178. [[CrossRef](#)]
38. Rinaldi, R.; Jastrzebski, R.; Clough, M.T.; Ralph, J.; Kennema, M.; Bruijnincx, P.C.; Weckhuysen, B.M. Paving the Way for Lignin Valorisation: Recent Advances in Bioengineering, Biorefining and Catalysis. *Angew. Chem. Int. Ed.* **2016**, *55*, 8164–8215. [[CrossRef](#)]
39. Dai, Z.; Ren, P.-G.; He, W.; Hou, X.; Ren, F.; Zhang, Q.; Jin, Y.-L. Boosting the electrochemical performance of nitrogen-oxygen co-doped carbon nanofibers based supercapacitors through esterification of lignin precursor. *Renew. Energ.* **2020**, *162*, 613–623. [[CrossRef](#)]

40. Taer, E.; Taslim, R.; Apriwandi, A. Ultrahigh Capacitive Supercapacitor Derived from Self-Oxygen Doped Biomass-Based 3D Porous Carbon Sources. *ChemNanoMat* **2022**, *8*, e202100388. [[CrossRef](#)]
41. Shi, F.; Tong, Y.; Li, H.; Li, J.; Cong, Z.; Zhai, S.; An, Q.; Wang, K. Synthesis of oxygen/nitrogen/sulfur codoped hierarchical porous carbon from enzymatically hydrolyzed lignin for high-performance supercapacitors. *J. Energy Storage* **2022**, *52*, 104992. [[CrossRef](#)]
42. Zhang, Y.; Fan, S.; Li, S.; Song, Y.; Wen, G. 3D porous oxygen-enriched graphene hydrogels with well-balanced volumetric and gravimetric performance for symmetric supercapacitors. *J. Mater. Sci.* **2020**, *55*, 12214–12231. [[CrossRef](#)]
43. García-Mateos, F.J.; Rosas, J.M.; Ruiz-Rosas, R.; Rodríguez-Mirasol, J.; Cordero, T. Highly porous and conductive functional carbon fibers from electrospun phosphorus-containing lignin fibers. *Carbon* **2022**, *200*, 134–148. [[CrossRef](#)]
44. Ding, J.; Wang, H.; Li, Z.; Kohandehghan, A.; Cui, K.; Xu, Z.; Zahiri, B.; Tan, X.; Lotfabad, E.M.; Olsen, B.C.; et al. Carbon Nanosheet Frameworks Derived from Peat Moss as High Performance Sodium Ion Battery Anodes. *ACS Nano* **2013**, *7*, 11004–11015. [[CrossRef](#)] [[PubMed](#)]
45. Shi, C.; Hu, L.; Guo, K.; Li, H.; Zhai, T. Highly Porous Carbon with Graphene Nanoplatelet Microstructure Derived from Biomass Waste for High-Performance Supercapacitors in Universal Electrolyte. *Adv. Sustain. Syst.* **2017**, *1*, 1600011. [[CrossRef](#)]
46. Fang, Y.; Luo, B.; Jia, Y.; Li, X.; Wang, B.; Song, Q.; Kang, F.; Zhi, L. Renewing functionalized graphene as electrodes for high-performance supercapacitors. *Adv. Mater.* **2012**, *24*, 6348–6355. [[CrossRef](#)] [[PubMed](#)]
47. Liu, J.; Wang, J.; Xu, C.; Jiang, H.; Li, C.; Zhang, L.; Lin, J.; Shen, Z.X. Advanced Energy Storage Devices: Basic Principles, Analytical Methods, and Rational Materials Design. *Adv. Sci.* **2018**, *5*, 1700322. [[CrossRef](#)]
48. Okhay, O.; Tkach, A. Graphene/Reduced Graphene Oxide-Carbon Nanotubes Composite Electrodes: From Capacitive to Battery-Type Behaviour. *Nanomaterials* **2021**, *11*, 1240. [[CrossRef](#)]
49. Gogotsi, Y.; Penner, R.M. Energy Storage in Nanomaterials—Capacitive, Pseudocapacitive, or Battery-like? *ACS Nano* **2018**, *12*, 2081–2083. [[CrossRef](#)]
50. Wang, M.; Liu, H.; Zhai, D.D.; Chen, X.Y.; Zhang, Z.J. In-situ synthesis of highly nitrogen, sulfur co-doped carbon nanosheets from melamine-formaldehyde-thiourea resin with improved cycling stability and energy density for supercapacitors. *J. Power Sources* **2019**, *416*, 79–88. [[CrossRef](#)]
51. Zhao, G.; Chen, C.; Yu, D.; Sun, L.; Yang, C.; Zhang, H.; Sun, Y.; Besenbacher, F.; Yu, M. One-step production of O-N-S co-doped three-dimensional hierarchical porous carbons for high-performance supercapacitors. *Nano Energy* **2018**, *47*, 547–555. [[CrossRef](#)]
52. Wan, X.; Shen, F.; Hu, J.; Huang, M.; Zhao, L.; Zeng, Y.; Tian, D.; Yang, G.; Zhang, Y. 3-D hierarchical porous carbon from oxidized lignin by one-step activation for high-performance supercapacitor. *Int. J. Biol. Macromol.* **2021**, *180*, 51–60. [[CrossRef](#)] [[PubMed](#)]
53. Karaaslan, M.A.; Lin, L.-T.; Ko, F.; Rennekar, S. Carbon Aerogels From Softwood Kraft Lignin for High Performance Supercapacitor Electrodes. *Front. Mater.* **2022**, *9*, 894061. [[CrossRef](#)]
54. Tian, J.; Liu, C.; Lin, C.; Ma, M. Constructed nitrogen and sulfur codoped multilevel porous carbon from lignin for high-performance supercapacitors. *J. Alloys Compd.* **2019**, *789*, 435–442. [[CrossRef](#)]
55. Du, B.; Zhu, H.; Chai, L.; Cheng, J.; Wang, X.; Chen, X.; Zhou, J.; Sun, R.-C. Effect of lignin structure in different biomass resources on the performance of lignin-based carbon nanofibers as supercapacitor electrode. *Ind. Crop. Prod.* **2021**, *170*, 113745. [[CrossRef](#)]
56. Du, B.; Wang, X.; Chai, L.; Wang, X.; Pan, Z.; Chen, X.; Zhou, J.; Sun, R.C. Fabricating lignin-based carbon nanofibers as versatile supercapacitors from food wastes. *Int. J. Biol. Macromol.* **2022**, *194*, 632–643. [[CrossRef](#)]
57. Thielke, M.W.; Lopez Guzman, S.; Victoria Tafoya, J.P.; García Tamayo, E.; Castro Herazo, C.I.; Hosseinei, O.; Sobrido, A.J. Full Lignin-Derived Electrospun Carbon Materials as Electrodes for Supercapacitors. *Front. Mater.* **2022**, *9*, 859872. [[CrossRef](#)]
58. Liang, Y.; Liu, X.; Qi, X. Hierarchical nanoarchitectonics of ordered mesoporous carbon from lignin for high-performance supercapacitors. *Int. J. Biol. Macromol.* **2022**, *213*, 610–620. [[CrossRef](#)]
59. Perera Jayawickramage, R.A.; Ferraris, J.P. High performance supercapacitors using lignin based electrospun carbon nanofiber electrodes in ionic liquid electrolytes. *Nanotechnology* **2019**, *30*, 155402. [[CrossRef](#)]
60. Gong, Y.; Li, D.; Luo, C.; Fu, Q.; Pan, C. Highly porous graphitic biomass carbon as advanced electrode materials for supercapacitors. *Green Chem.* **2017**, *19*, 4132–4140. [[CrossRef](#)]
61. Park, J.H.; Rana, H.H.; Lee, J.Y.; Park, H.S. Renewable flexible supercapacitors based on all-lignin-based hydrogel electrolytes and nanofiber electrodes. *J. Mater. Chem. A* **2019**, *7*, 16962–16968. [[CrossRef](#)]
62. Chen, Y.; Zhang, G.; Zhang, J.; Guo, H.; Feng, X.; Chen, Y. Synthesis of porous carbon spheres derived from lignin through a facile method for high performance supercapacitors. *J. Mater. Sci. Technol.* **2018**, *34*, 2189–2196. [[CrossRef](#)]
63. Zhang, Y.; Zhao, C.; Ong, W.K.; Lu, X. Ultrafast-Freezing-Assisted Mild Preparation of Biomass-Derived, Hierarchically Porous, Activated Carbon Aerogels for High-Performance Supercapacitors. *ACS Sustain. Chem. Eng.* **2018**, *7*, 403–411. [[CrossRef](#)]
64. Lin, T.; Chen, I.W.; Liu, F.; Yang, C.; Bi, H.; Xu, F.; Huang, F. Nitrogen-doped mesoporous carbon of extraordinary capacitance for electrochemical energy storage. *Science* **2015**, *350*, 1508–1513. [[CrossRef](#)]
65. Li, Y.; Wang, G.; Wei, T.; Fan, Z.; Yan, P. Nitrogen and sulfur co-doped porous carbon nanosheets derived from willow catkin for supercapacitors. *Nano Energy* **2016**, *19*, 165–175. [[CrossRef](#)]
66. Cao, Y.; Chen, S.S.; Zhang, S.; Ok, Y.S.; Matsagar, B.M.; Wu, K.C.; Tsang, D.C.W. Advances in lignin valorization towards bio-based chemicals and fuels: Lignin biorefinery. *Bioresour. Technol.* **2019**, *291*, 121878. [[CrossRef](#)] [[PubMed](#)]